Published in final edited form as:
J Aerosol Sci. 2010 November 1; 41(11): 1030–1043. doi:10.1016/j.jaerosci.2010.06.005.

Airflow and nanoparticle deposition in rat nose under various breathing and sniffing conditions:

a computational evaluation of the unsteady effect

Jianbo Jiang[a] and **Kai Zhao**[a]
[a] Monell Chemical Senses Center, Philadelphia, PA 19104

Abstract

Accurate prediction of nanoparticle (1~100 nm) deposition in the rat nasal cavity is important for assessing the toxicological impact of inhaled nanoparticles as well as for potential therapeutic applications. A quasi-steady assumption has been widely adopted in the past investigations on this topic, yet the validity of such simplification under various breathing and sniffing conditions has not been carefully examined. In this study, both steady and unsteady computational fluid dynamics (CFD) simulations were conducted in a published rat nasal model under various physiologically realistic breathing and sniffing flow rates. The transient airflow structures, nanoparticle transport and deposition patterns in the whole nasal cavity and the olfactory region were investigated and compared with steady state simulation of equivalent flow rate. The results showed that (1) the quasi-steady flow assumption for cyclic flow was valid for over 70% of the cycle period during all simulated breathing and sniffing conditions in the rat nasal cavity, or the unsteady effect was only significant during the transition between the respiratory phases; (2) yet the quasi-steady assumption for nanoparticle transport was not valid, except in the vicinity of peak respiration. In general, the total deposition efficiency of nanoparticle during cyclic breathing would be lower than that of steady state due to the unsteady effect on particle transport and deposition, and further decreased with the increase of particle size, sniffing frequency, and flow rate. In the contrary, previous study indicated that for micro-scale particles (0.5~4μm), the unsteady effect would increase deposition efficiencies in rat nasal cavity. Combined, these results suggest that the quasi-steady assumption of nasal particle transport during cycling breathing should be used with caution for an accurate assessment of the toxicological and therapeutic impact of particle inhalation. Empirical equations and effective steady state approximation derived in this study are thus valuable to estimate such unsteady effects in future applications.

Keywords

Computational Fluid Dynamics; Rat nasal cavity; Nanoparticle deposition; Olfactory region; Cycling breathing

Jianbo Jiang Address: Monell Chemical Senses Center 3500 Market Street Philadelphia, PA 19104-3308, USA Phone Number: (267) 519-4937 Fax Number: (215) 898-2084 jjiang@monell.org
Kai Zhao Address: Monell Chemical Senses Center 3500 Market Street Philadelphia, PA 19104-3308, USA Phone Number: (267) 519-4935 Fax Number: (267) 519-4935 kzhao@monell.org

1. INTRODUCTION

The nasal cavity is the first line of defense in the respiratory tract that filters out inhaled airborne particulate matters thus protecting the delicate low airways (Balásházy, Hofmann, & Heistracher, 2003). On the other hand, the deposition of therapeutic particles or droplets in the nasal cavity has been used for clinical treatment of allergies, congestion, blood disorders, migraine headache, and osteoporosis etc (Mathison, Nagilla, & Kompella, 1998). In recent years, the transport and deposition of nanoparticles (diameter less than or equal to 100 nm) is of increasing concern since nanoparticles are more toxic and diffusible than larger particles (Oberdorster et al., 2004), while its utilization may improve the therapeutic delivery efficiency of the drugs (Illum, 2002).

Laboratory rats are commonly used as human surrogates to investigate the inhalation toxicology and applied pharmacology. Extrapolation from the particle deposition data in animal models allows the estimation of delivered dosage of inhaled particles to target sites in the human nasal cavities by taking into account the structural differences. Thus detailed and accurate information about the particle deposition in the rat nasal cavity is an important step towards this goal.

The complexities in geometry and the small dimensions of the rat nasal cavity have made the direct in vivo studies of airflow difficult, instead, in vitro models (Morgan et al., 1991) and in-silica models (Kimbell et al., 1997; Yang, Scherer, & Mozell, 2007; Zhao, Dalton, Yang, & Scherer, 2006; Minard et al., 2006) have been the mainstay for the investigation. Results generated from the in vitro and computational approaches generally agree with each other - that for inspiration, airflow enters into the caudal central domain then diverges into parallel and complex dorsal, lateral and ventral channels. Streamlines that enters dorsal channel generally follow an “S-Shape” route into the olfactory ethmoid recesses, while such S-shaped streamlines become less prevalent during expiration (Yang, Scherer, & Mozell, 2007; Zhao, Dalton, Yang, & Scherer, 2006; Minard et al., 2006). However, in order to significantly reduce the temporal complexity of the computational or experimental setup when analyzing the flow dynamics and transport phenomena, all the above studies employed a common quasi-steady state approximation that assumes nasal airflow is time-independent. The assumption is based on theoretical dimensionless analysis of Womersley and Strouhal number for respiratory airflow in the rat nasal cavity (Grotberg, Sheth, & Mockros, 1990). Most of these studies also assumed laminar flow condition, while only one report argued that rat nasal airflow has non-laminar components based on the measured pressure drops at different flow rates (Cheng et al., 1990).

Similarly, the quasi-steady assumption was widely applied when investigating transport and deposition of nanoparticles in the rat nasal cavities in vivo (Wolff, Kanapilly, Gray, & McClellan 1984; Gerde, Cheng, & Medinsky, 1991; Martonen & Yang, 1990), in plastic nasal molds (Cheng et al., 1990) and computationally (Garcia & Kimbell, 2009). These steady state results generally agree well with each other – that the overall nasal deposition efficiency decreases with increase of flow rate and particle size (ranging from 5 nm to 200 nm) during inspiration, while expiratory flow results in slightly higher pressure drop and lower deposition efficiency than inspiratory flow. The spatial deposition patterns for the smaller nanoparticles (for example, 3 nm) are mainly aggregated in the anterior region, but expand more uniformly with the increase of particle size and flow rate. Under quasi-steady assumption, Zhao, Dalton, Yang, & Scherer (2006) and Yang, Scherer, Zhao, & Mozell (2007) investigated the deposition (uptake) and transport of odorant molecules (whose typical diameter is less than 1 nm) with different water solubility in the rat nasal cavity. One of their important finding is that the increase of airflow pass through the olfactory region during inspiration than expiration may lead to differences between inspiratory and expiratory olfactory activity (Scott, Acevedo,

Sherrill, & Phan, 2007). Furthermore, insoluble odorant molecules were found to deposit more uniform along the nasal cavity than that of the soluble ones, mimicking the effect of particles sizes.

The above review of the literature clearly indicates that detailed information on airflow and nanoparticle transport in rat nasal cavities is mostly obtained under the assumption of quasi-steady states. However, in reality, air flow through rat nose is not steady but characterized by deceleration and acceleration of a wide range of flow rates and altering frequencies, ranging from 2 Hz at resting state to 12 Hz at strong sniffing (Youngentob, Mozell, Sheehe, & Hornung, 1987). The theoretical dimensionless analysis of the Womersley number and Strouhal number (Yang, Scherer, & Mozell, 2007; Yang, Scherer, Zhao, & Mozell, 2007) may not be sufficient to neglect the effects of unsteadiness in all regions, nor has its validity been fully investigated for nanoparticle transport. In related topics, such as the deposition of micro-particles (0.5 to 4 μm), which are dominated by inertial impaction, were found through both in vivo and in vitro rodent studies (Kelly, Bobbitt, & Asgharian, 2001; Kelly, Kimbell, & Asgharian, 2001) to be markedly higher under unsteady pulsatile flows than that of steady state flows. For human upper airway (Zhang & Kleinstreuer, 2004) and nasal cavity (Shi, Kleinstreuer, & Zhang, 2006), computational study indicated that unsteadiness of nanoparticle transport cannot be neglected especially during the deceleration phase of inspiratory cycle and the total deposition was found to be lower than that of steady case with equivalent flow rate. Velocity measurements in a symmetric bifurcation human lung model under cyclic conditions (Lieber & Zhao, 1998) showed that even quasi-steady assumption for airflow may not always be valid, in this case, only in the vicinity of peak exhalation.

The current paper is devoted to the computational investigation of transport and deposition of nanoparticles in a rat nasal cavity under different physiological realistic breathing rates. We will especially examine the unsteadiness effects on the airflow pattern and nanoparticle transport/deposition when compared to steady state results, and derive empirical equations to capture such transient effects, if necessary.

2. Materials and methods

2.1 Mesh generation

A published computational model of the rat nasal passage (Figure 1(a); Yang, Scherer, & Mozell, 2007; Yang, Scherer, Zhao, & Mozell, 2007) was used in this study. It was developed from a polymer cast of a Sprague-Dawley rat right nasal cavity. The cast was sectioned horizontally on a milling machine to produce 88 longitudinal sections which were used to construct the 3D anatomically accurate computational grid by using the CFD software package FIDAP® (Ansys, Inc., Canonsburg, PA). In the present study, the original FIDAP grid was imported into FLUENT (Ansys, Inc., Canonsburg, PA) with no alteration of geometry and mesh quality, confirmed by comparison at different coronal and horizontal cross sections. The final grid contained 134,014 nodes and 107,024 brick elements. Grid-independence study was conducted on three finer grids (225,196, 533,884, and 955,179 elements) by using Fluent solution-adaptive mesh refinement feature. It turned out that the results of velocity and particle concentration were already converged on the original grid level (107,024 elements).

2.2 Breathing pattern

Three physiological flow conditions - restful breathing, moderate sniffing, and strong sniffing (Youngentob, Mozell, Sheehe, & Hornung, 1987) were simulated under both unsteady and quasi-steady state in this study. The related kinematic data is summarized in the Table 1. The sniff frequency in rat increases from 2–4 Hz during the normal restful breathing to 8–12 Hz during strong sniffing when exploring novel odors. In most part of the present study, the

respiration breathing pattern for the unsteady simulation was assumed to be sinusoidal (Figure 1(b)). The actual sniffing pattern in rat is not sinusoidal, but consists of varying shapes of inspiration and expiration profiles, with periods of apnea in between. The use of sinusoidal sniffing waves serves to simplify our numerical computation cost, and such simplification will be validated by simulation of one in vivo recorded sniffing trace in an awake rat (Figure 1(c); (Cheung Carey, & Wachowiak, 2009)) that contains both low and high sniffing frequencies.

2.3 Governing equations and boundary conditions

The continuity and momentum equations for the airflow take the following forms under the laminar flow, incompressible, and isothermal assumption (300 K):

$$\frac{\partial u_i}{\partial x_i}=0 \tag{1}$$

$$\frac{Du_i}{Dt}=\frac{\partial u_i}{\partial t}+u_j\frac{\partial u_i}{\partial x_j}=-\frac{1}{\rho}\frac{\partial p}{\partial x_i}+\nu\frac{\partial^2 u_i}{\partial x_j\partial x_j} \tag{2}$$

where u_i, p and ν are the i^{th} component of the velocity vector, pressure, and air kinetic viscosity, respectively.

Nanoparticles ranging from 1 nm to 100 nm were considered in this study, and assumed to be sufficiently dilute with negligible effects on airflows. The particle concentration was then modeled by advection-diffusion equation, ignoring coagulation, aggregation, surface growth, nucleation, gravity, and other internal and external forces:

$$\frac{\partial c}{\partial t}+u_i\frac{\partial c}{\partial x_i}=D_a\frac{\partial^2 c}{\partial x_i\partial x_i} \tag{3}$$

where D_a is the molecular diffusivity of particles in the air and is calculated from the Stokes-Einstein equation (Clift, Grace, & Weber, 1978).

For steady case, uniform velocity and particle concentration were specified at the inlet (external naris during inspiration and nasopharyngeal end during expiration). Previous numerical study (Yang, Scherer, & Mozell, 2007) have confirmed that flow field in the downstream is not significantly affected by the inlet velocity profile for a given flow rate. At the outlet (nasopharyngeal end during inspiration and external naris during expiration), zero-gradient of velocity, pressure and particle concentration (Dirichlet condition) was applied. All the walls were assumed to be non-slip (zero velocity) with perfectly absorbing surfaces (zero particle concentration) for the nanoparticles.

The cyclic flow rate profile (Figure 1(b)) was specified at the inlet (external naris) by the following expression:

$$Q=Q_0\sin(2\pi f_0 t) \tag{4}$$

where Q is the transient flow rate, Q_0 is the peak flow rate, and f_0 is the frequency. The values of Q_0 and f_0 used in this study are listed in Table 1. The other boundary conditions for cyclic case were same as those for steady case, that is, uniform particle concentration at the inlet

(external naris), Dirichlet condition at the outlet (nasopharyngeal end), and non-slip, perfectly absorbing walls.

2.4 Numerical methods

The numerical solutions of the continuity, momentum, and particle transport equations were carried out with commercial finite-volume based, unstructured solver, FLUENT (ANSYS, Inc., Canonsburg, PA). The computational domain was divided into control volumes where the variables, including velocity components, pressure, and particle concentrations, were located at the centroid of the control volume. The differential form of the governing equations was integrated over each control volume to construct algebraic equations for the discrete variables. Second-order upwind scheme was used to discretize the spatial dimensions and second order implicit scheme was employed to model the time derivative. Finally the pressure and velocity correlations were solved using the SIMPLE method (Pantakar, 1980).

The converged solutions were assumed to be obtained when the scaled residuals of continuity, momentum, and particle transport equations, were less than 10^{-5} for mass and momentum, and 10^{-9} for particle concentration. The global quantities including wall shear stresses on the walls and average particle concentration at the outlet were also monitored to check the convergence. It was found that the criteria of scaled residuals specified above were enough for solution convergence and improving the convergence criteria had a negligible effect on the simulation results.

Validation of computational fluid dynamics (CFD) simulations with existed experimental data is necessary so that CFD can be used with confidence and the simulation results can be considered reliable. The CFD models were validated with measured nanoparticle deposition in a tube and rat nasal cavity (Jiang & Zhao, 2009).

3. Results and Discussions

3.1 Transient vs. steady airflow

The transient inspiratory and expiratory streamlines patterns (see Figure 2(a), t = 1/10T and Figure 2(b), 9/10T, restful breathing condition, where T is the cycling period) are similar to those from quasi-steady flow simulation (Kimbell et al., 1997; Yang, Scherer, & Mozell, 2007) and flow visualization (Morgan et al., 1990). In briefly, flow streams released from dorsal medial side of the external naris traced out S-shape curves and passed through the olfactory recess during inspiration. Those released from ventral medial side flowed along the floor of the nasal cavity. Streamlines passing through the dorsal lateral meatus and ventral lateral meatus originated from the dorsal lateral side and ventral lateral side of the external naris. During expiration, much less streamlines entered the olfactory region than inspiratory flow.

For both inspiration and expiration (see Figure 2(c), t = 1/10T and Figure 2(d), 9/10T, restful breathing condition), the primary axial airflow occurs ventrally, in the nasopharyngeal meatus, with a second peak velocity in the dorsal recess, which are consistent with previous steady state studies (Kimbell et al., 1997; Yang, Scherer, & Mozell, 2007). The axial velocity distribution patterns were quantitatively and qualitatively compared at four coronal planes and found to be similar between transient inspiratory acceleration (t=1/10 T), deceleration (t=4/10T) and steady state, all of which have the same flow rate. The differences of velocity at the four planes between the three phases were evaluated by the normalized mean square error (NMSE) (ASTM, 2002). The NMSE values were calculated to be less than 0.07, indicating good agreement between the velocity profiles of the three phases. Same observations apply for the expiratory phase at t=6/10T and 9/10T, and for the two other sniffing conditions. Thus, it seems that the transient effects on rat nasal airflows are negligible and the flow field

can be approximated as quasi-steady. However, significant differences of velocity distribution were found between acceleration phase, deceleration phase, and steady case with equivalent flow rate near the transition between respiratory phases, for example, t=1/100T or 99/100T, indicating the non-negligible effects of flow unsteadiness.

What has not been described in details in previous literature are the secondary motion of rat nasal flows, which are induced by curvature, directional changes and rapid expansion of the nasal passages. The secondary flow would extract momentum from the primary (axial) flows, reduce primary velocity, increase the residence time of the inhaled nanoparticles, enhance the lateral mixing of the mass and momentum, and therefore, strongly affect the nanoparticle deposition in the nasal cavities. Figure 3 shows the secondary flow (indicated by arrows) for the inspiratory acceleration (Figure 3(a), t=1/10T) and expiration deceleration (Figure 3(b), t=9/10T) during restful breathing. In the anterior part the nose (plane1), secondary flows were predicted to move away from septum and flow into meatus during inspiration but move towards to septum and/or flow out of meatus during expiration. In the posterior regions, where the olfactory recess is mostly located (plane 2–4), the secondary flows were found to move mainly downwards towards the nasal floor during inspiration and upwards towards the nasal roof during expiration. The strength of the secondary flow (*SS*) is defined as the ratio of secondary flow velocity to total velocity, $SS=\sqrt{\frac{v^2+w^2}{u^2+v^2+w^2}}$, where *u* is the velocity component in the main (axial) flow direction, and *v* and *w* are the velocity components in the plane perpendicular to *u*. Figure 3 shows that *SS* is consistently stronger in the posterior regions than the anterior ones during both inspiration and expiration, which may affect the nanoparticle deposition in the olfactory region. In accordance with to axial velocity distribution, secondary flow fields during acceleration (t=1/10T) and deceleration (t=4/10T) are quite similar to those of steady state flow with equivalent flow rate in the region far away from transition between respiratory phases.

The effects of unsteadiness on the developing flows in finite length channels can be estimated by the Womersley number W_0 (Womersley, 1955) and the Strouhal number *S* (Schroter & Sudlow, 1969):

$$W_0=R\left(\frac{2\pi f}{\nu}\right)^{1/2},\ S=\frac{2\pi fL}{U} \tag{5}$$

where R is the hydraulic diameter of the external naris, *f* is the cycling frequency, ν is the air kinematic viscosity, L is the axial length along the nasal cavity, and U is the average velocity during one cycle or instantaneous velocity at the external naris. By definition, the Womersley number is a dimensionless ratio of the unsteady inertial forces in relation to viscous forces. Whereas, the Strouhal number, which is derived from the ratio of the steady boundary layer thickness to the Stokes layer thickness (Pedley, Schroter, & Sudlow, 1977), represents the ratio of unsteady inertial forces or local acceleration to the convective inertial forces. Quasi-steady flow can be assumed as long as W_0 is less than 4 and *S* is less than 1 (Isabey & Chang, 1981). For the present rat nasal airway, the values of W_0 and *S* based on average velocity were estimated to be 1.45, 2.64, 3.73 and 0.33, 0.53, 0.54 for restful breathing, moderate sniffing and strong sniffing, respectively. Although these values seems to meet the criteria of flow quasi-steadiness (W_0 <4 and *S* <1), the aforementioned flow unsteadiness near the respiratory transition indicates that Strouhal number based on average velocity can not adequately characterize flow states. Instead, Strouhal number based on instantaneous velocity is more appropriate, as shown in Figure 4, which is a Moody plot of non-dimensionalized pressure drop versus the Reynolds number for the three unsteady respiratory conditions and steady flows

during inspiration (Figure 4(a)) and expiration (Figure 4(b). It is evident from Figure 4 that unsteadiness is significant only near the transition between inspiration and expiration, and negligible near peak flow. More specifically, the quasi-steady assumption is valid for about 84%, 76%, and 72% of the cycling period for restful breathing, moderate sniffing, and strong sniffing respectively. Furthermore, Figure 4 also shows that resistance during the deceleration is lower than during the acceleration for both inspiratory and expiratory flows when the unsteady effects are significant, indicating energy dissipation during the respiratory cycle. Such hysteresis of pressure loss has been reported in the human rhinomanometry measurements (Sullivan & Chang, 1991). Finally Figure 4 indicates that, near the transition of respiratory phases (smaller Re number), unsteady flows during the deceleration deviate more from steady flows than those during acceleration for both inspiration and expiration.

3.2 Transient vs. steady nanoparticle transport and deposition

We applied the same strategy to compare the nanoparticle transport and deposition at various acceleration phases (for example, t = 1/10T and 2/10T), deceleration phases (for example, t =3/10T and 4/10T) and steady state to examine the unsteady effects. If the quasi-steady assumption for particle transport would hold, there wouldn't be any significant difference in either the deposition flux or concentration field between these paired conditions, which all has the same flow rate. However, the differences observed (Figure 5, deposition flux of 1 nm particles on the septal wall) are significant for t=1/10T vs. t=4/10T (Figure 5(a)), with more particles reaching the downstream during deceleration (t=4/10T) than that during acceleration (t=1/10T) and the steady state. The differences are likely to be resulted from temporal separation of momentum and mass transport that more nanoparticles are inhaled into nasal cavity during the interval between t=1/10T and t=4/10T due to the higher flow rate than that during the interval of 0~1/10T, which results in accumulation of particles within the airstream, and subsequently higher deposition. The accumulation effect weakens near the peak of inspiration, for example, at t=2/10T and. t=3/10T, where the particle deposition pattern and concentration is quite similar to that of quasi steady state (Figure 5(b)). Similar effects were also observed during the expiratory phase. Thus, the quasi-steady assumption of 1 nm nanoparticle transport in rat nasal cavity at restful breathing is only valid in the temporal period far away enough from the respiratory transition, in other words, near the vicinity of respiration peaks. This is similar to flow field but the quasi-steadiness temporal period of nanoparticles is shorter, as seen from above observations. Furthermore, the quasi-steadiness period becomes even shorter with increase of nanoparticle size and changing from restful breathing to moderate and strong sniffing. For example, when particle size increases from 1 nm to 2.78 nm for the restful breathing, or when restful breathing changes to moderate sniffing for 1 nm particles, the differences of concentration distribution between t=2/10T (or 3/10T) and steady case become significant. Within a even narrower temporal window, for example, t=2.3~ 2.7/10T for moderate sniffing for 1 nm particles, and t=2.45 ~ 2.65/10T for strong sniffing for 2.78 nm particles, good agreement can still be found for the unsteady and equivalent steady state in concentration field.

The validity of quasi-steadiness of nanoparticle field is also spatially dependent. For example, the concentration of 100 nm particles at the peak inspiration during strong sniffing was significantly different from that of steady case with equivalent flow rate in the posterior nasal region (e.g. plane 4, see Figure 2(a) or Figure 2(b)). On the other hand, the concentration distributions of unsteady and steady cases in the anterior nasal region (plane 1, see Figure 2(a) or Figure 2(b)) were still similar, indicating the validity of quasi-steadiness of particle field in this region. Furthermore, it was found that this spatial region expands from anterior towards posterior nasal cavity with decrease of particle size. Similar trend was found when changing from moderate sniffing to restful breathing or from strong sniffing to moderate sniffing.

3.3 Transient vs. steady nasal deposition dosimetry as a function of nanoparticle size and breathing conditions

CFD simulations were used to calculate the deposition dosimetry as a function of particles size and breathing rate, a further comparison of the unsteady effects. Figure 6 summarizes such function for the whole nasal cavity (Figure 6(a)) and olfactory region (Figure 6(b)) for both steady and unsteady state. The unsteady state deposition was averaged over the inhalation cycle and the average flow rate for the given inhalation cycle was used for the steady case. The deposition efficiency for whole nasal cavity decreases with the increase of particle size and flow rates for both cyclic and steady cases. Particle diffusivity is reversely proportional to the particle size so larger nanoparticles have lower deposition efficiency. Increase of breathing rates decreases the residence time of nanoparticles in the nasal cavity thus reduces the opportunities to deposit onto the wall. Thus larger deposition efficiency is found for lower breathing flow rate. While, the deposition efficiency for cyclic flow is lower than those for steady case. The reduction increases with nanoparticle size and flow rate. For example, deposition efficiency in cyclic restful breathing condition of 1 nm, 10 nm, and 100 nm nanoparticles decreases about 4%, 20%, and 40%, as compared to their equivalent steady state flow.

For deposition to the olfactory region, there exists an optimal particle size for maximum deposition rate. The optimal size decreases with the increase of flow rate. For example, for steady conditions, it decreases from 5 nm at restful breathing to 3 nm at strong sniffing. The increase of flow rate results in higher deposition efficiency before maximal deposition but the trend is reversed after maximal deposition. Similarly, deposition efficiency for the cyclic case is slight higher (lower) than those of steady case before (after) reaching the maximal values. The above observation can be explained by the counter-acting effects of particle diffusivity, particle concentration remaining in the airstream when entering the olfactory region, and residence time of particles in the olfactory region. For a given flow rate, smaller nanoparticles (for example, 1 nm or 2 nm) deposit more in the anterior region than large nanoparticles (3 nm, 5 nm or 100 nm) and thus less remaining in the airstream when enter the olfactory region. On the other hand, larger nanoparticles are less diffusive than smaller nanoparticles and hence have less deposition efficiency than smaller nanoparticles. The counter-balancing effects resulted in an optimal particle size for maximal deposition. Similarly, as the flow rate increases, less nanoparticles deposit in the anterior region and more nanoparticles remain in the airflows entering the olfactory region; while the particle residence time in the olfactory region decreases with increase of flow rate. These effects combined resulted in the increase of deposition efficiency in the olfactory region for smaller nanoparticles but decreases for large ones with the increase of flow rate. Thus, smaller optimal particle size is reached for higher flow rates.

One reason for the reduction of particle deposition efficiency during cyclic flow is the increase of flow rate near the peak flow. Within the inspiratory cycle, the flow rate in the period between t=0.22T and t=0.39T is higher than that steady flow rate which is about 64% of peak flow rate of cyclic flow. Using the deposition equations for steady flow (See Equation (5) in the following text) and assuming that particle deposition in infinitely small time is steady, integration of instantaneous deposition over the inspiratory period of a cycle during moderate sniffing gives deposition efficiency lower than steady case but higher than cyclic case (Figure 6(a)). This indicates that the increase of flow rate near the peak inspiration can not adequately account for the reduction of particle deposition during cyclic flows. It should be noted that the above integration assumes the instantaneous particle deposition is in the same phase with cyclic flows.

Figure 7 depicts the variation of instantaneous deposition (normalized by peak value) with particle size and flow rate during the inspiration phase of one cycle. During restful breathing for 1 nm nanoparticle, the position of maximum instantaneous deposition rate is very close to that of peak inspiration (t=T/4). With increase of particle size and/or change of respiratory

condition from restful breathing to sniffing, the position of maximal deposition rate moves away from peak inspiration and towards deceleration phase. At the same time, the instantaneous deposition rate curve becomes highly unsymmetrical and much higher deposition rate is found during the deceleration than acceleration phase. At the end of inspiration, the instantaneous deposition rate doesn't decrease to zero and takes higher value for larger particles and/or stronger respiratory conditions. The deposition rate during the acceleration is lower than the deceleration especially for larger nanoparticles and higher flow rate/sniffing frequency. Figure 7 also explains why decreased diffusion effects near peak inspiratory flow alone cannot account for the deduction of deposition during cyclic breathing conditions: the particle deposition curve deviates from the inflow pattern (sinusoid) with increase of particle size and/or changing from restful breathing to sniffing conditions. In other words, the phase shift (defined as time interval between the point when peak flow rate is reached and the one when deposition rate reaches the maximal) and non-zero deposition at the start/end of inspiration increase with particle size and breathing conditions.

Changing from restful breathing to sniffing is associated with an increase in both flow rate and breathing frequency (Table 1). It is desirable to investigate the individual effects of these two factors on the particle deposition and transport. A series of computations (results not shown here), assuming sinusoidal inflow, were conducted for 10 nm particles at constant frequency (5 Hz) but variable peak flow rates (100~1000 ml/min), and constant peak flow rate (252 ml/min) but variable frequency (1.5~10 Hz). It was found that phase shift increased with frequency but decreases with peak flow rate. Combined with increasing effects of particle size under the same breathing condition (restful breathing, moderate sniffing, or strong sniffing) shown in Figure 7, the phase shift is the net result of competing effects of particle size, peak flow rate, and cycling frequency, or in non-dimensional form, proportionally related to the particle Strhouhal number ($Str_C\, Sc^{1/3} S$, where Sc is the Schmidt number (ν/D) and D is the diffusion coefficient of particle in air, Grotberg, Sheth, & Mockros, 1990). Nonetheless, the phase shift is not determined by the Str_C number alone but also the depends on the Str number, W_0 number (Equation (5)). Figure 7 shows that strong sniffing has larger phase shift and non-zero deposition at the start/end of inspiration than moderate sniffing although they have similar Str_C numbers for given particle sizes (Table 2). Noting that both flow rate and frequency were doubled from moderate sniffing to strong sniffing and the value of W_0 number during strong sniffing was larger than during moderate sniffing, thus the variations in frequency more significantly affected the phase shift than flow rate.

The potential value and future application for this study lies in if we can use CFD models to calculate the deposition dosimetry as a function of particles size and breathing conditions, with correction for the unsteady effects. Thus, empirical equations are then fitted to characterize the nanoparticle deposition rates in both whole nasal cavity and olfactory region taking into account the steady and cyclic breathing conditions. The equation for whole nasal cavity deposition function takes the form of:

$$\eta = C_1\left[1 - \exp(-C_2 D^{0.517} Q^{-0.45})\right]^{C_3} \tag{6}$$

Where D is the particle diffusivity, Q is the flow rate, C_i (i=1, 2, 3) is fitted coefficient. By fitting equation (6) to the simulated deposition data, values of C_i (i=1, 2, 3) were obtained with mean and standard deviation as follows: C_1=0.99±0.005, C_2=12.26±0.2, C3=1.47±0.06 for steady flow, and C_1=0.95±0.007, C_2=10.48±0.3, C_3=1.47±0.07 for cyclic flow. The R^2 values for the fit are greater than 0.99 (Figure 8(a)). In a similar way, Cheng et al. (1990) and Garcia and Kimbell (2009) derived the deposition models for nanoparticles through the rat nasal cavity during only steady inspiratory flows based on either experimental data and simulated results, where slightly different equation forms (compared with (6)) were adopted: $D^{0.517}Q^{-0.234}$ for

Cheng et al (1990) and $D^{0.36}Q^{-0.606}$ in Garcia and Kimbell (2009). The difference in the diffusion parameter may be attributed to the different nasal cavities adopted in the studies. For example, pharynx and larynx were included in the rat nasal cavities of Cheng et al (1990) but not in our model and that of Garcia and Kimbell (2009).

The regional deposition in the olfactory region can be fitted with the log-normal equation:

$$\eta_{olf}=\frac{C_1 Q^{C_2}}{\sqrt{2\pi}}\exp\left[-\frac{1}{2Q^{C_2}}\left(\ln\left(\frac{D}{C_3}\right)\right)^2\right] \quad (7)$$

The values of C_i (i=1,2, 3) are calculated as C_1=3.878±0.512, C_2=−0.051±0.004, C_3=16.585 ±1.517 for steady flow, and C_1=4.636±0.824, C_2=−0.048±0.005, C_3=10.874±1.229 for cyclic flow. The R^2 values for the fit are greater than 0.96 (Figure 8(b)).

For future applications, these fitted equations (6) and (7) with appropriate set of C values can be potentially used to derive deposition efficient for a wide range of particle size and sniffing conditions under both unsteady and steady flow conditions, without changing the base form of the equation.

Since unsteady simulations of nasal airflow and nanoparticle deposition are much more computationally expensive than steady ones, it would be valuable to derive an empirical effective flow rate that can estimate the averaged nanoparticle deposition efficiency during breathing cycles based on steady case of that effective flow rate. From Figure 6(a), it can be concluded that such effective flow rate (matching flow rate) should be higher than the average cyclic flow rate but lower than peak inspiration flow rate:

$$Q_{effective}=C(Q_{average}+Q_{peak}) \quad (8)$$

For micro-particles deposition in a triple bifurcation lung airway model (Zhang & Kleinstreuer, 2004) and for nanoparticle deposition in a human nose (Shi, Kleinstreuer, & Zhang, 2006), previous studies have derived C to be a constant of 0.5. Based on our results, the value of C varies with particle size: 0.5 for smaller nanoparticles (<1 nm), but decrease to 0.4 for larger nanoparticles (>1 nm). The agreement between simulation and prediction with matching flow rate is good (see Figure 9): the R^2 values for the prediction are greater than 0.99 in the whole nasal cavity (Figure 9(a)) and 0.95 in the olfactory region (Figure 9(b)). A comparison of Figure 8(b) and Figure 9(b) shows that prediction with matching flow rate agrees slightly better with simulation than empirical equation (7) in the olfactory region.

3.4 Sniffing of awake rats

In the above analysis, the air flow rate at the external naris during breathing was simplified to a cyclic sinusoid. To validate such simplification, a series of simulations were conducted based on in vivo measurements of an awake rat sniffing (Figure 1(c); (Cheung, Carey, & Wachowiak, 2009)) that consists of both high frequency, high flow rate (strong sniffing) and low frequency, low flow rate (restful breathing). The general conclusions from sinusoid simulation still hold for that of the real sniffing trace. For example, the airflow field is still quasi-steady for major part of the cycle but not for the nanoparticle field. Figure 10 shows the deposition rate normalized by maximal deposition during two inspiration phases for higher frequency and low frequency sniffing respectively, in which the high frequency sniffing profile actually resembles a sinusoid. Similar to Figure 7, increase of breathing frequency and particle size tends to result in higher deposition during the deceleration phase and larger phase shift between peak flow and maximal deposition. The temporal window where quasi-steadiness of particle

concentration field can be assumed is around the peak inspiration and decreases in width with particle size and frequency. The spatial region of quasi-steady particle concentration field during inspiration is located in the anterior nasal cavity and shrinks with particle size and frequency. The finding confirms that the sinusoid can be used as the building block to describe and approximate periodic profiles of breathing and sniffing in rat.

3.5 Turbulent or laminar rat nasal airflows

The above simulations were conducted under the assumption that rat nasal airflows are laminar flows. Although the maximal Reynolds number based on velocity at the external naris and its diameter is less than 2300 for the respiratory conditions considered in this study, this can not guarantee the laminar nature of rat nasal airflow. The complicated anatomy of rat nasal passages consisting of diverging and converging conduits may make the transition from laminar flows to turbulent flows to occur at a Reynolds number considerably below the critical value of 2300. The pressure drop measured by Cheng et al (1990) in rat nasal casts was found to vary nonlinearly with flow rate. However, this non-linearity in the pressure-flow rate relationship can not exclude the validity of laminar assumption either since laminar flow can also show such nonlinear variation. To evaluate possible turbulent effects in the rat nasal cavity, inspiratory airflow during steady strong sniffing (Table 1) was simulated with the Large Eddy Simulation (LES) with dynamical subgrid model (Germano, Piomelli, Moin, & Cabot, 1991) implemented in Fluent (Ansys, Inc., Canonsburg, PA). The advantage of dynamical LES over traditional RANS turbulence models (Wilcox, 1998) lies in its ability for accurate prediction of the full range of flow types, laminar, transitional, and turbulent flows (Germano, Piomelli, Moin, & Cabot, 1991). Grid independence study was performed to determine an acceptable grid resolution to use for strong sniffing. The grid with 2,116,059 elements, which resolves over 80% of the turbulent kinetic energy through the nasal cavity, produced similar pressure drop across the nasal cavity and velocity profiles at certain locations as that with 1,782,194 elements, indicating an adequate grid resolution (Pope, 2000). The results from 2,116,059 element grid simulation showed that velocity distributions derived from dynamical LES were basically identical to those from laminar model. Furthermore, even imposing some turbulent fluctuations in the external naris, they diminished very quickly in the anterior skin region and were basically zero in the main nasal cavity. Since the flow rate of strong sniffing is highest among the three respiratory breathing conditions considered in this study (Table 1) and transition to turbulence only occurs at high flow rate, the laminar flow assumption is also valid for the moderate sniffing and restful breathing.

4. Summary and Conclusion

In this paper we have simulated the steady and cycling airflow, transport and deposition of nanoparticles (1 nm~100 nm) based on a published anatomically accurate right nasal cavity under the restful breathing, moderate sniffing, and strong sniffing conditions. The main results of airflow and nanoparticle transport from present study are summarized as follows:

1. The quasi-steady assumption of the nasal airflow field is valid over 70% of the cycle period. The unsteady effects can not be neglected only during the transition between the respiratory phases. We further provided detailed characterization of the distribution of secondary flows;
2. The quasi-steady assumption for the particle concentration fields is not valid due to the accumulative effects (Shi, Kleinstreuer, & Zhang, 2006): more nanoparticles drift towards posterior portion of nasal cavity during deceleration phase than steady case and result in higher particle concentration. On the other hand, the acceleration phase receives the less nanoparticle deposition than steady case. Furthermore, the accumulation effects are less significant in the vicinity of peak inspiration than the

regions near the transition between inhalation, and less significant in anterior than posterior of nasal cavity during inspiration;

3. For both steady state and cyclic flows, total deposition efficiencies of nanoparticles in the whole nasal cavity decrease with increase of particle size and flow rate, and there exists one optimal nanoparticle size where maximal deposition efficiency in the olfactory region is reached. However, the total deposition efficiency during cyclic flows is lower than those of steady flows. In contrast, it has been reported that the total deposition efficiency of micro-scale particles increases due to the transient effect (Kelly, Kimbell, & Asgharian, 2001);

4. The quasi-steady assumption for the particle concentration fields should be used with caution. The spatial and temporal regions where this assumption is valid depend on particle size, flow rate, and breathing frequency, and thus on the particle Strouhal number (Str_C). More specifically, the temporal region is limited in the vicinity of peak inspiration and decreases towards peak inspiration with increase of particle size and changing from restful breathing to sniffing. The spatial region occupies approximately the whole nasal cavity for tiny nanoparticle such as 1 nm particles but decrease towards anterior region during inspiration with increase of particle size and changing from restful breathing to sniffing;

5. We have suggested two ways to simplify the estimation of unsteady effect on the deposition and transport of nanoparticles in the whole nasal cavity and olfactory region, either using the empirical equations (see equations (6) and (7)) or using the steady state effective flow rate (see equation (8)) if the user have some computational capability, which seems to provide more accurate prediction in the olfactory region than the empirical equations;

6. We showed that rat nasal airflow is basically laminar flow under the breathing conditions considered in this study by using the Large Eddy Simulation with dynamic subgrid model (Germano, Piomelli, Moin, & Cabot, 1991). Further experiments are needed to verify this conclusion. Finally, limitations of the present study should be mentioned. All the simulations assumed the perfect absorption of particle on the wall and did not take into account the mucus movement. Another limitation of this study is that only nanoparticle was considered. Recent experimental studies of larger particles (>1μm) showed the significant effects of breathing pattern on the particle deposition in the rat nasal cavity (Kelly, Kimbell, & Asgharian, 2001). These remain to be included in future studies.

Acknowledgments

We thank Dr. Matt Wachowiak at the Department of Biology, Boston University, for providing the in vivo awake rat sniffing trace recoding, and Dr. Scherer at the Department of Bioengineering, University of Pennsylvania, for discussion.

References

ASTM. Annual Book of American Society for Testing Materials Standards. American Society for Testing Materials; West Conshohocken: 2002. Standard guide for statistical evaluation of indoor air quality models (D5157-97); p. 23-34.

Balásházy I, Hofmann W, Heistracher T. Local particle deposition patterns may play a key role in the development of lung cancer. Journal of Applied Physiology 2003;94:1719–1725. [PubMed: 12533493]

Cheng YS, Hansen GK, Su YF, Yeh HC, Morgan KT. Deposition of ultrafine aerosols in rat nasal molds. Toxicology and Applied Pharmacology 1990;106:222–233. [PubMed: 2256113]

Cheung MC, Carey RM, Wachowiak M. A Method for Generating Natural and User-Defined Sniffing Patterns in Anesthetized or Reduced Preparations. Chemical Senses 2009;34:63–76. [PubMed: 18791186]

Clift, R.; Grace, JR.; Weber, ME. Bubble, Drops and Particles. Academic Press; New York: 1978.

Garcia GJM, Kimbell JS. Deposition of inhaled nanoparticles in the rat nasal passages: Dose to the olfactory region. Inhalation Toxicology 2009;21:1165–1175. [PubMed: 19831956]

Gerde P, Cheng YS, Medinsky MA. Invivo deposition of ultrafine aerosols in the nasal airway of the rat. Fundamental and Applied Toxicology 1991;16:330–336. [PubMed: 2055363]

Germano M, Piomelli U, Moin P, Cabot WH. A dynamic subgrid-scale eddy viscosity model. Physics of Fluids 1991;3:1760–1765.

Grotberg JB, Sheth BV, Mockros LF. An analysis of pollutant gas-transport and absorption in pulmonary airways. Journal of Biomechanical Engineering-Transactions of the ASME 1990;112:168–176.

Illum L. Nasal drug delivery: new developments and strategies. Drug Discovery Today 2002;7:1184–1189. [PubMed: 12547019]

Isabey D, Chang HK. Steady and unsteady pressure-flow relationships in central airways. Journal of Applied Physiology 1981;51:1338–1348. [PubMed: 7298472]

Jiang, JB.; Zhao, K. Deposition of inhaled particles in the olfactory region in rat and human nasal cavities during breathing. 31th Annual Meeting of Association for Chemoreception Sciences (AChemS); Sarasota, Florida, USA. April 22–26; 2009.

Kelly JT, Bobbitt CM, Asgharian B. In vivo measurement of fine and coarse aerosol deposition in the nasal airways of female Long-Evans rats. Toxicological Sciences 2001a;64:253–258. [PubMed: 11719708]

Kelly JT, Kimbell JS, Asgharian B. Deposition of fine and coarse aerosols in a rat nasal mold. Inhalation Toxicology 2001b;13:577–588. [PubMed: 11452355]

Kimbell JS, Godo MN, Gross EA, Joyner DR, Richardson RB, Morgan KT. Computer simulation of inspiratory airflow in all regions of the F344 rat nasal passages. Toxicology and Applied Pharmacology 1997;145:388–398. [PubMed: 9266813]

Lieber BB, Zhao Y. Oscillatory flow in a symmetric bifurcation airway model. Annals of Biomedical Engineering 1998;26:821–830. [PubMed: 9779955]

Martonen TB, Yang Y. Simulation of aerosol deposition in extrathoracic and laryngeal passages of the laboratory rat. Journal of Aerosol Science 1993;24:103–113.

Mathison S, Nagilla R, Kompella UB. Nasal route for direct delivery of solutes to the central nervous system: Fact or fiction? Journal of Drug Targeting 1998;5:415–441. [PubMed: 9783675]

Minard KR, Einstein DR, Jacob RE, Kabilan S, Kuprat AP, Timchalk CA, Trease LL, Corley RA. Application of magnetic resonance (MR) imaging for the development and validation of computational fluid dynamic (CFD) models of the rat respiratory system. Inhalation Toxicology 2006;18:787–794. [PubMed: 16774868]

Morgan KT, Kimbell JS, Monticello TM, Patra AL, Fleishman A. Studies of inspiratory air-flow patterns in the nasal passages of the f344 rat and rhesus-monkey using nasal molds - relevance to formaldehyde toxicity. Toxicology and Applied Pharmacology 1991;110:223–240. [PubMed: 1891770]

Oberdorster G, Sharp Z, Atudorei V, Elder A, Gelein R, Kreyling W, Cox C. Translocation of inhaled ultrafine particles to the brain. Inhalation Toxicology 2004;16:437–445. [PubMed: 15204759]

Pantakar, V. Numerical heat transfer and fluid flow. McGraw-Hill; New York: 1980.

Pedley, TJ.; Schroter, RC.; Sudlow, MF. Gas Flow and Mixing in the Airway. In: West, JB., editor. Bioengineering Aspects of the Lung. Marcel Dekker; New York: 1977. p. 163-265.

Pope, SB. Turbulent Flows. Cambridge University Press; Cambridge, England: 2000.

Schroter RC, Sudlow MF. Flow patterns in models of human bronchial airways. Respiration Physiology 1969;7:341–355. [PubMed: 5823844]

Scott JW, Acevedo HP, Sherrill L, Phan M. Responses of the rat olfactory epithelium to retronasal air flow. Journal of Neurophysiology 2007;97:1941–1950. [PubMed: 17215498]

Shi H, Kleinstreuer C, Zhang Z. Laminar airflow and nanoparticle or vapor deposition in a human nasal cavity model. Journal of Biomechanical Engineering-Transactions of the ASME 2006;128:697–706.

Sullivan KJ, Chang HK. Steady and oscillatory transnasal pressure-flow relationships in healthy-adults. Journal of Applied Physiology 1991;71:983–992. [PubMed: 1757337]

Wilcox, DC. Turbulence modeling for CFD. DCW Industries Inc; La Canada, CA: 1998.

Wolff RK, Kanapilly GM, Gray RH, McClellan RO. Deposition and retention of inhaled aggregate (ga203)-ga-67 particles in beagle dogs, fischer-344 rats, and cd-1 mice. American Industrial Hygiene Association Journal 1984;45:377–381. [PubMed: 6741792]

Womersley JR. Method for the calculation of velocity, rate of flow and viscous drag in arteries when the pressure gradient is known. Journal of Physiology-London 1955;127:553–563.

Yang GC, Scherer PW, Mozell MM. Modeling inspiratory and expiratory steady-state velocity fields in the Sprague-Dawley rat nasal cavity. Chemical Senses 2007;32:215–223. [PubMed: 17220519]

Yang GC, Scherer PW, Zhao K, Mozell MM. Numerical modeling of odorant uptake in the rat nasal cavity. Chemical Senses 2007;32:273–284. [PubMed: 17220517]

Youngentob SL, Mozell MM, Sheehe PR, Hornung DE. A quantitative-analysis of sniffing strategies in rats performing odor detection tasks. Physiology & Behavior 1987;41:59–69. [PubMed: 3685154]

Zhang Z, Kleinstreuer C. Airflow structures and nano-particle deposition in a human upper airway model. Journal of Computational Physics 2004;198:178–210.

Zhao K, Dalton P, Yang GC, Scherer PW. Numerical modeling of turbulent and laminar airflow and odorant transport during sniffing in the human and rat nose. Chemical Senses 2006;31:107–118. [PubMed: 16354744]

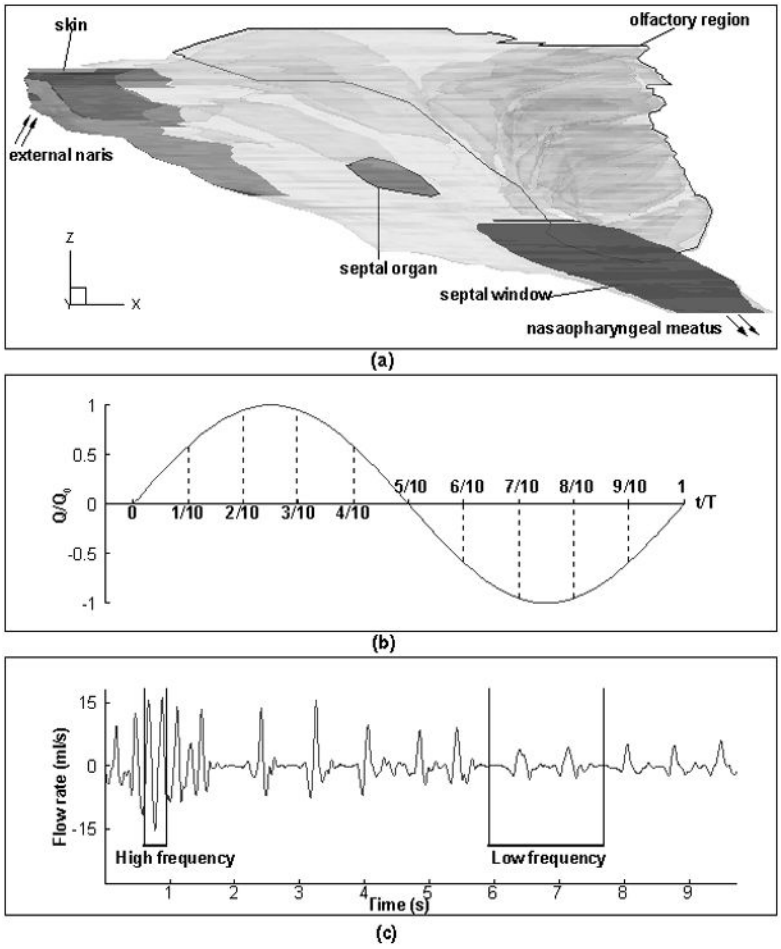

Figure 1.
(a) Geometry of rat nasal cavity; (b) sinusoidal breathing simplification (See text for more details); (c) real rat sniffing trace.

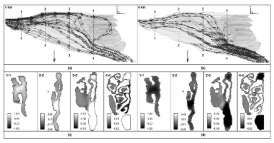

Figure 2.
Streamlines in rat nasal cavity during (a) acceleration, inspiration (1/10T) and (b) deceleration, expiration (9/10T); and axial velocity distributions at (c)1/10T and (d) 9/10T in 4 coronal sections (section1- section 4) as indicated in Figure 2(a–b) during restful breathing (Unit: m/s).

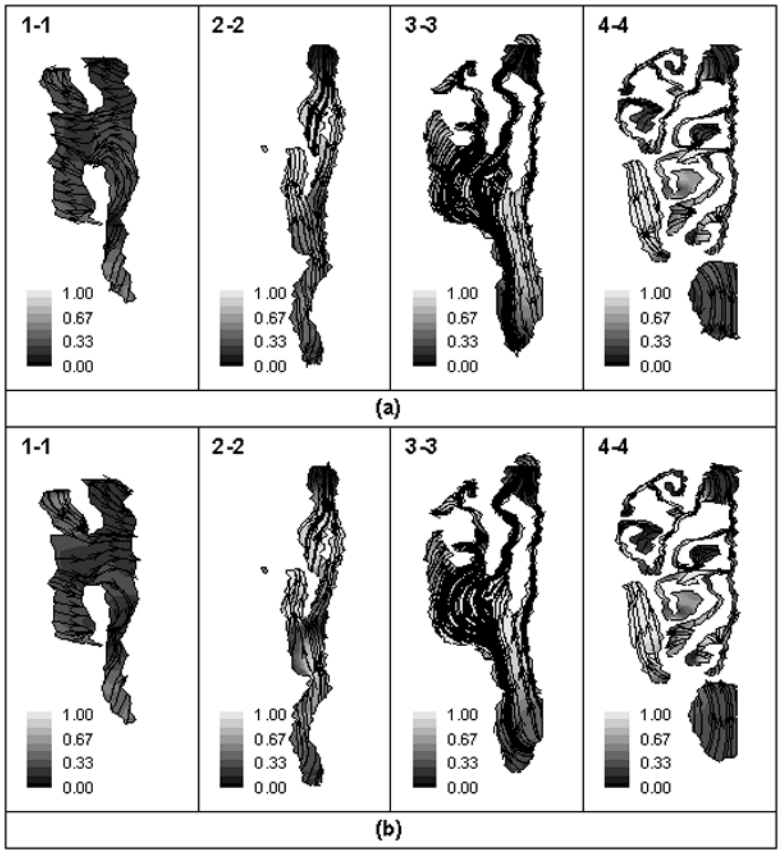

Figure 3.
Vector plots and strength iso-contours of secondary flow in coronal sections (section1- section 4) at (a) 1/10T (inspiration; top) (b) 9/10T (expiration; bottom) during restful breathing.

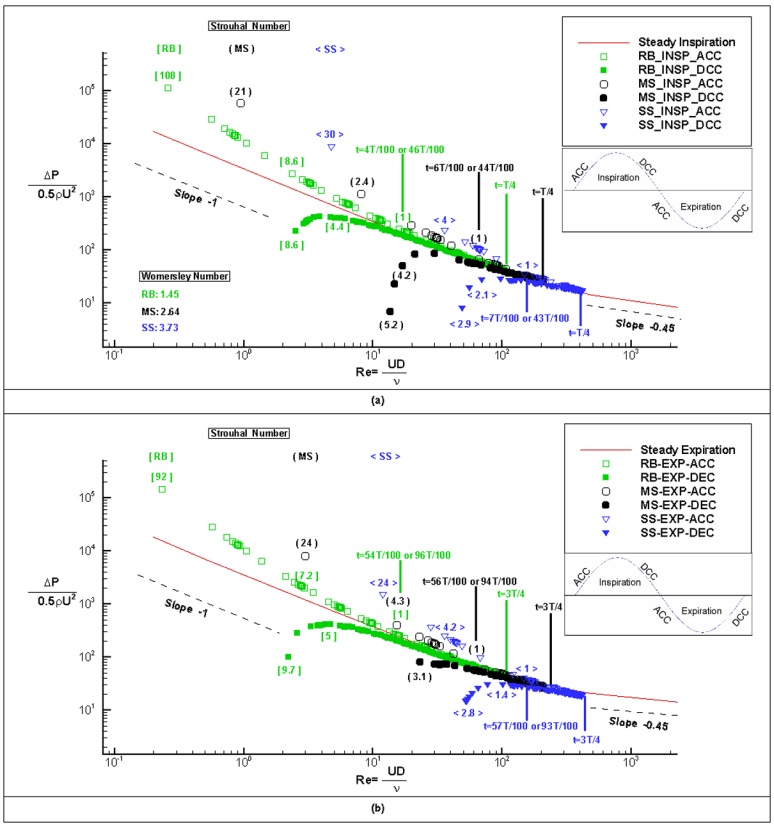

Figure 4.

Moody diagram of the non-dimensionalized pressure drop vs. Reynolds number. The data are plotted for both inspiratory flow (a, top plot) and expiratory flow (b, bottom plot) under the three unsteady respiratory breathing conditions (Restful breathing: RB, Moderate sniffing: MS, and Strong sniffing: SS). Solid lines represent steady flows. Values of Womersley number and Strouhal number are computed from Equation (5) in text.

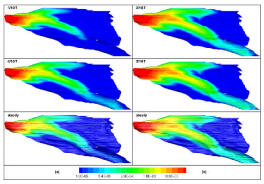

Figure 5.
Deposition flux of 1 nm particles on the nasal cavity during inspiration at airflow rate of 74 mL/min (Left column; during acceleration--t=1/10T, deceleration--t=4/10T, and steady state) and 119 mL/min (Right column; during acceleration--t=2/10T, deceleration--t=3/10T, and steady state) during restful breathing (Septal view) (Unit: $g/cm^2/s$).

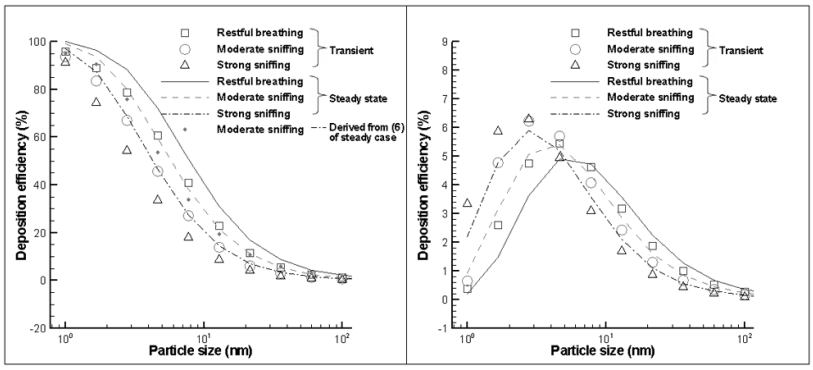

Figure 6.
Comparison the total deposition efficiency between transient and equivalent steady case in the whole nasal cavity (a, left) and Olfactory region (b, right).

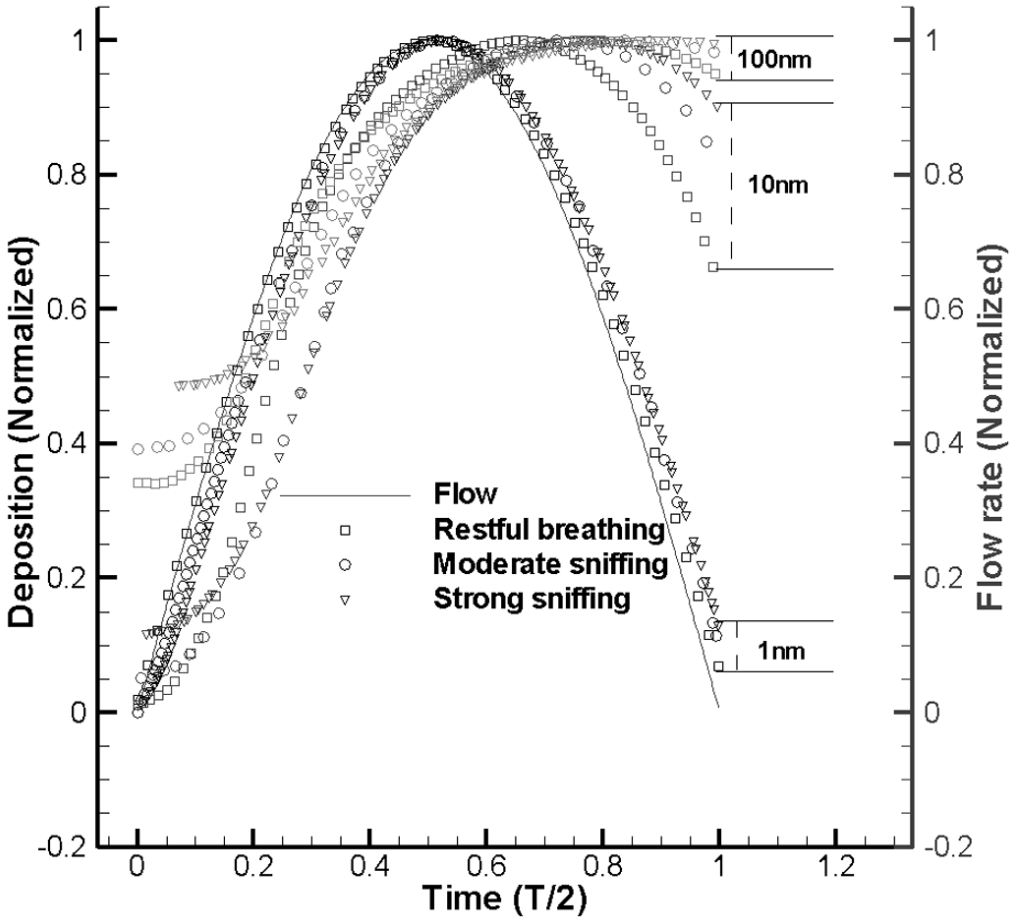

Figure 7.
Normalized depositions during inspiration phase in one cycle.

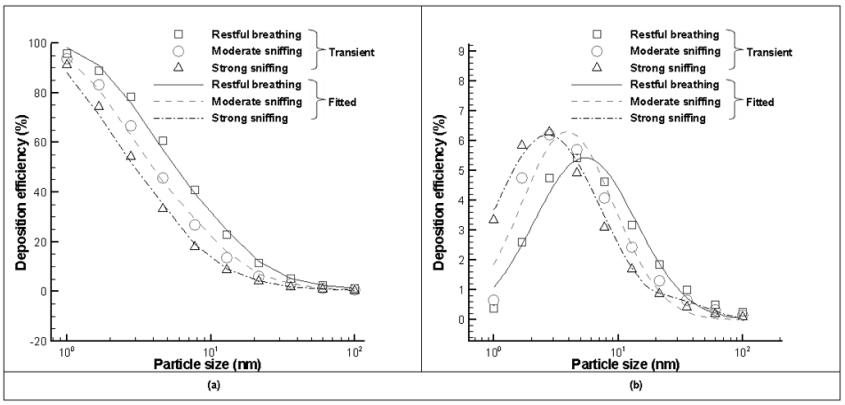

Figure 8.

Comparisons of nanoparticle deposition efficiency in the whole nasal cavity (a, left) and olfactory region (b, right) under cyclic breathing conditions and those with fitted equations (6) and (7) respectively.

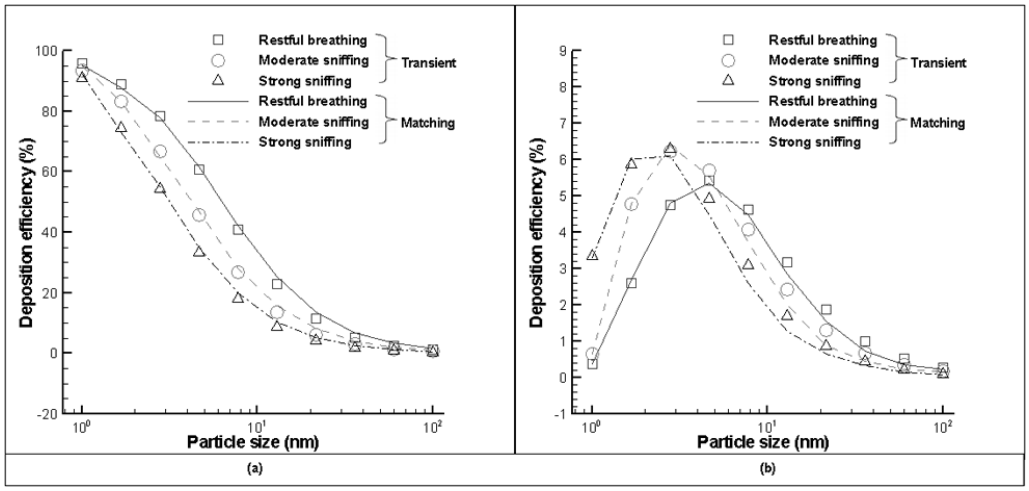

Figure 9.
Comparisons of nanoparticle deposition efficiency in the whole nasal cavity (a, left) and olfactory region (b, right) under cyclic breathing and effective steady conditions.

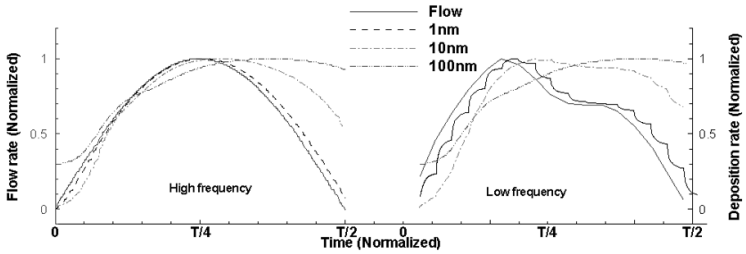

Figure 10.
Normalized depositions during inspiration phase for the real sniffing trace.

Table 1

Flow parameters. Note that the values of steady airflow rate are the volumetric average flow rates of corresponding cyclic breathing patterns.

	Sinusoid			Real trace	
	Restful Breathing	**Moderate Sniffing**	**Strong Sniffing**	**Low Frequency**	**High Frequency**
Steady	Q=80 (ml/min)	Q=160 (ml/min)	Q=321 (ml/min)	–	–
Cyclic	Q_0 =126 (ml/min), f_0 =1.5 (Hz)	Q_0 =252 (ml/min), f_0 =5 (Hz)	Q_0 =504 (ml/min), f_0 =10 (Hz)	Q_0 =229 (ml/min), f_0 =2.85 (Hz)	Q_0 =914 (ml/min), f_0 =5 (Hz)

Table 2

Average Particle Strouhal number (Str_C)

	Sinusoid			Real Trace	
Particle Size (nm)	**Restful Breathing**	**Moderate Sniffing**	**Strong Sniffing**	**Low Frequency**	**High Frequency**
1	0.29	0.47	0.48	0.3	0.13
1.67	0.41	0.67	0.68	–	–
2.78	0.57	0.94	0.95	–	–
4.64	0.80	1.32	1.33	–	–
7.74	1.12	1.86	1.87	–	–
10	1.27	2.61	2.62	1.63	0.71
21.54	2.20	3.65	3.66	–	–
35.94	3.32	5.51	5.52	–	–
59.95	4.20	6.98	6.99	–	–
100	5.70	9.46	9.48	5.91	2.57